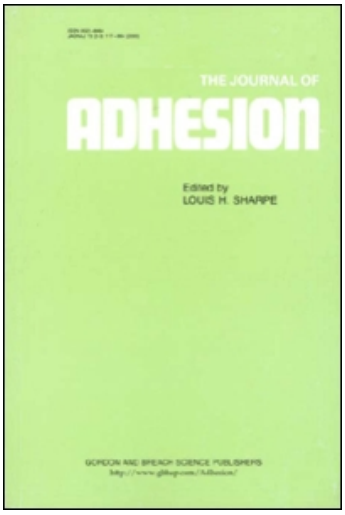

The Journal of Adhesion
Publication details, including instructions for authors and subscription information:
http://www.informaworld.com/smpp/title~content=t713453635

Creep Effects in Nanometer-scale Contacts to Viscoelastic Materials: A Status Report

W. N. Unertl[a]
[a] Department of Physics and Laboratory for Surface Science and Technology, University of Maine, Orono, ME, USA

To cite this Article Unertl, W. N.(2000) 'Creep Effects in Nanometer-scale Contacts to Viscoelastic Materials: A Status Report', The Journal of Adhesion, 74: 1, 195 — 226
To link to this Article: DOI: 10.1080/00218460008034530
URL: http://dx.doi.org/10.1080/00218460008034530

J. Adhesion, 2000, Vol. 74, pp. 195 - 226
Reprints available directly from the publisher
Photocopying permitted by license only

Creep Effects in Nanometer-scale Contacts to Viscoelastic Materials: A Status Report

W. N. UNERTL*

Department of Physics and Laboratory for Surface Science and Technology, University of Maine, Orono, ME 04469, USA

(Received 17 August 1999; In final form 21 December 1999)

Effects of creep on the behavior of nanometer-scale contacts to viscoelastic materials are described from the viewpoint of the contact mechanics theory developed by Ting. The two most important effects are: (1) The time at which maximum contact area and maximum deformation occur can be delayed substantially from the time of maximum applied load. (2) The deformation at separation is related to the loss tangent. These long-range effects due to creep are distinct from the much shorter-range crack tip effects induced by adhesion at the periphery of the contact and associated with the names Barquins and Maugis. Consideration of relevant time scales reveals that creep effects are expected to dominate in SFM-scale contacts for a wide range of compliant viscoelastic materials. Guidelines for selection of optimal experimental parameters for nanometer-scale studies are presented. The need for a comprehensive theory is emphasized.

Keywords: Viscoelastic materials; Nanomechanics; Contact deformation; Contact mechanics; Scanning force microscope

1. INTRODUCTION AND BACKGROUND

There is increasing need for quantitative measurements of properties of materials with nanometer-scale resolution. Applications include materials characterization [1, 2], microelectromechanical systems and tribology [3 - 7], and biological systems [8]. At present, the scanning force microscope (SFM) [1] is the predominant method for such

*Tel.: 207-581-2251, Fax: 207-581-2255, e-mail: unertl@maine.edu

measurements although other techniques are promising [9]. In SFM, the indenter is a sharp tip that is contacted to the sample and the mechanical response measured. The edge of the contact is frequently pictured as the tip of a crack [10, 11] so that any increase or decrease in contact size is equivalent to the closing or opening of a crack at the contact periphery. The SFM tip shape is usually modeled as a paraboloid of revolution $f(r) = r^2/2R_o$ where $f(r)$ is the height at radius r and R_o is the radius of curvature at the point of contact [12, 13]. Figure 1a compares a parabolic profile with a typical dimension for SFM tips ($R_o = 50\,\text{nm}$) with spherical profiles of radii 50 nm. Cylindrical coordinates (r, z) are used. Notation used to describe the contacts is shown in Figure 1b for a rigid parabolic probe in contact with an initially-flat, perfectly-elastic substrate under time-dependent

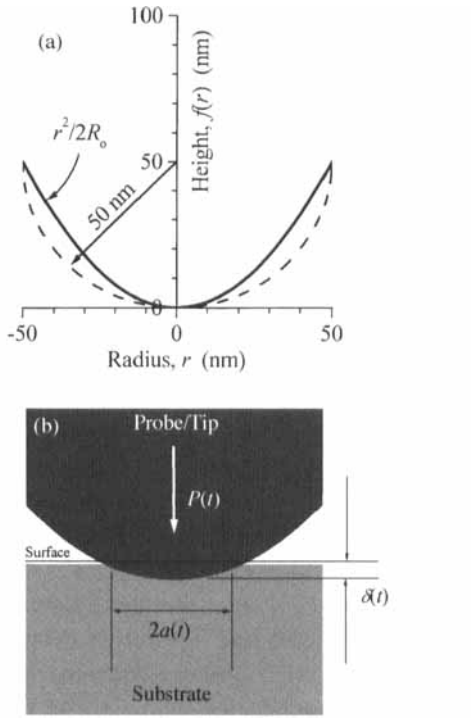

FIGURE 1 (a) Parabolic profile used to model the SFM probe (solid line) compared with a spherical profiles with a radius R_o; (b) Geometry of a deformable contact between an axially-symmetric, rigid probe and flat surface.

load $P(t)$. The radius of the circular contact is $a(t)$ and the rate at which it changes is $V = da/dt$; $\delta(P, t)$ is the deformation along the symmetry axis. Mechanical properties such as modulus, yield strength, and work of adhesion are extracted from the SFM data using continuum mechanics models from the field of contact mechanics [14, 15]. These models include adhesion and are very well developed for contacts between elastic materials [16].

Unfortunately, the appropriate contact mechanics analysis is not yet completed for viscoelastic materials. However, Johnson [17] has recently identified two limiting regimes, each with a characteristic response time. In this chapter, these regimes will be called the *crack regime* and the *creep regime* and their characteristic times the crack relaxation time, τ_{crack}, and the creep relaxation time, τ_{creep}. In the creep regime, bulk deformations due primarily to the Hertz contact pressure are dominant and the effects of adhesion are neglected. Since the contact radius, a, characterizes the range of creep deformations,

$$\tau_{\text{creep}} \approx a/\langle V \rangle \tag{1}$$

where $\langle V \rangle$ is the average value of V. In the late 1960's, Ting [18, 19] solved the creep problem for cases where adhesion can be neglected. More recently, Wahl, Stepnowski and Unertl reported creep effects in SFM studies of 1,2 polybutadiene [20, 21]. The primary purpose of this article is to describe the application of the Ting theory to nanometer-scale contacts.

In the crack regime, viscoelastic response is limited to a narrow zone at the periphery of the contact and long-range deformations are treated elastically; *i.e.*, creep effects are completely ignored. The theoretical description of the crack regime was developed by Barquins and Maugis [22, 23]. They incorporated viscoelastic response into the fracture mechanics approach to contact mechanics. The crack length, l, provides a measure of the range of crack tip effects so that

$$\tau_{\text{crack}} \approx l/\langle V \rangle. \tag{2}$$

Barquins and Maugis validated their model experimentally for macroscopic contacts to polyurethane [10, 22, 23]. Basire and Fretigny [24] used SFM to study the engulfment of the SFM probe into a

styrene-butadiene copolymer in the absence of any applied load. This process is driven entirely by adhesion forces [25].

Since $l \leq a$, $\tau_{\text{crack}} \leq \tau_{\text{creep}}$ [17]. For SFM-scale contacts to compliant materials the difference is expected to be large, so that $\tau_{\text{crack}} \ll \tau_{\text{creep}}$ [26]. Thus, in SFM, one expects the response of the contact to be dominated by the regime whose relaxation time is closest to the relaxation time of the viscoelastic material under study. Furthermore, both τ_{crack} and τ_{creep} can be varied over wide ranges by increasing or decreasing the total contact time, t_{contact} and, thus, changing $\langle V \rangle$.

The experimental range of t_{contact} accessible in quantitative SFM experiments is fairly large, typically from a fraction of a 1 ms to about 1000 s. The longest contact times are limited by thermal drift and creep of the piezoelectric elements. The shortest times are limited by cantilever response times and roll-off frequencies of electronic filters. Measurements can also be affected by mechanical resonances and frequency-dependent phase shifts of the instrument. These instrumental limitations, and others [8, 12], must be quantitatively understood before reliable measurements of mechanical properties can be made. Contact radii are typically in the range $1\,\text{nm} \lesssim a \lesssim 100\,\text{nm}$ for the probe tips and loads normally used in SFM experiments. Thus, the average rate of change of the contact radius $\langle V \rangle \equiv (da/dt)$ lies in the range $0.001\,\text{nm/s} \lesssim \langle V \rangle \lesssim 100\,\mu\text{m/s}$. This overlaps the range of some macroscopic contact experiments, which typically have $\langle V \rangle \gtrsim 1\,\mu\text{m/s}$ [23].

The major goal of this paper is to provide an overview of current understanding of the role that creep plays in the formation of contacts with nanometer-scale dimensions. The primary theoretical formulation of viscoelastic contact mechanics, due to Ting, is reviewed.

Quantitative examples based on simple mechanical models are used to illustrate the creep effects expected in dynamic SFM loading experiments. Some of these results have been presented previously [20, 21]. The major limitation of the Ting theory is its neglect of adhesion. Approaches to include adhesion, at least approximately, are discussed. Considerations for design of SFM experiments to emphasize either the creep or crack regimes are presented. Much of the material also applies to ultra-low-load indentation experiments like those of Asif, Wahl and Colton [9].

2. CONTACT MECHANICS FOR VISCOELASTIC MATERIALS IN THE ABSENCE OF ADHESION

Viscoelastic effects become important whenever contact dimensions change in a time interval that is comparable with a characteristic relaxation time, τ, of the viscoelastic material. Ting [18], following earlier work by Lee and Radok [27] and Graham [28], obtained a general solution to the equilibrium Hertz contact problem for the case of a *rigid axisymmetric* probe with shape $f(r)$ and an *isotropic* substrate with *linear viscoelastic* response. This response will be referred to as creep. He assumed a linear viscoelastic stress–strain ($\sigma_{ij} - \varepsilon_{ij}$) relation of the form

$$\sigma_{ij}(t) = \int_0^t [2G(t-\tau)\partial\varepsilon_{ij}(\tau)/\partial\tau + \delta_{ij}\lambda(t-\tau)\partial\varepsilon_{kk}(\tau)/\partial\tau]d\tau \qquad (3)$$

where $G(t)$ and $\lambda(t)$ are time-dependent relaxation moduli. $G(t)$ is the relaxation modulus in shear. The bulk modulus $K(t)$, the Poisson's ratio, $\nu(t)$, and the Young's modulus, $E(t)$, are all time dependent and related to $G(t)$ and $\lambda(t)$ by $K(t) \equiv \lambda + (2/3)G$, $\nu(t) \equiv (1/2)(3K - 2G)/(3K + G)$ and $E(t) \equiv 9KG/(3K + G)$ [29]. The lower limit 0^- allows for discontinuous jumps in stresses and strains at $t = 0$. Ting obtained explicit expressions for the contact radius, $a(t)$, and the penetration, $\delta(t)$, of the tip of the indenter assuming the following boundary conditions at $z = 0$:

$$\left.\begin{aligned} &\sigma_{zz} = \sigma_{rz} = 0 && r > a(t) \\ &u_z(r,t) = \delta(t) - f(r)H(t) \quad \text{and} \quad \sigma_{rz} = 0 && r \le a(t) \end{aligned}\right\} \qquad (4)$$

where $u_z(r,t)$ are the vertical displacements under the indenter in the z-direction and $H(t)$ is the Heavyside step function. These boundary conditions, Eq. (4), assume the stress component in the interface to be zero. This condition can be met either if the contact is frictionless or if the probe and substates have identical mechanical properties, requirements that are probably seldom met in real contacts. However, at least in the case of elastic contacts, failure to satisfy this condition leads to errors of only a few percent in contact radius and pull-off force [14, 30]. The z-axis coincides with the symmetry axis of the

indenter, is directed into the sample, and has its origin at the undeformed surface of the sample. These boundary conditions assume no adhesion and no friction at the interface between the indenter and sample. The solutions can be expressed in terms of two functions, $\phi(t)$ and $\psi(t)$, whose Laplace transforms are related by $s\hat{\psi}(s) = 1/s\hat{\phi}(s) = s\hat{G}(s)/[1 - s\hat{\nu}(s)]$. If the Poisson's ratio, ν, is assumed constant, $\psi(t)$ has the same form as $G(t)$, the relaxation modulus in shear, and $\phi(t)$ has the same form as the creep compliance in shear [18, 29].

The specific form of the solutions depends on whether the contact radius, $a(t)$, increasing or decreasing and whether it is larger or smaller than its value at $t = 0$. Figure 2 shows the three cases of interest here. The initial contact radius is a_o. Non-zero a_o can occur two ways. (1) The contact can reach equilibrium following application of a load in the distant past. (2) The viscoelastic response has a perfectly elastic component as is the case for the Maxwell and standard solid models. In case I (Fig. 2), $a(t)$ is increasing ($t \leq t_{\max}$) and the solution confirms the earlier result of Lee and Radok [27] which was based on the Boltzmann principle of correspondence [29]. Specifically, for

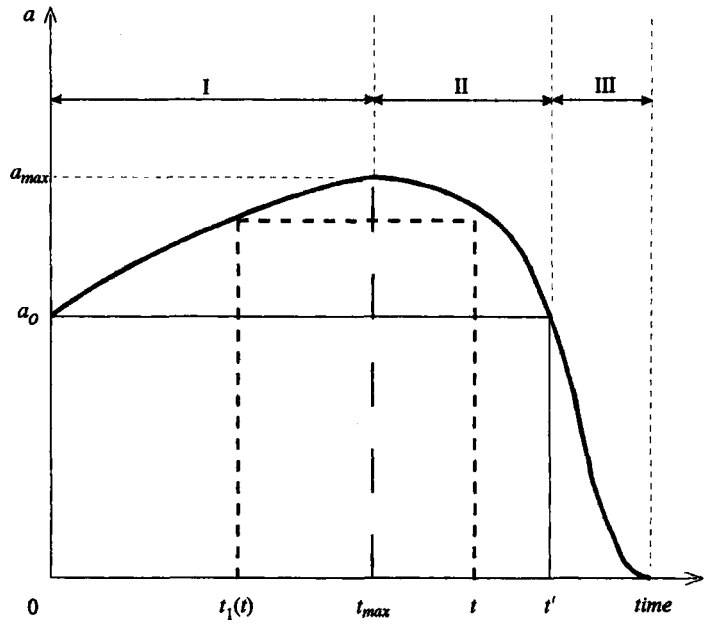

FIGURE 2 Variation of contact radius with contact time.

a parabolic indenter with $f(r) = r^2/2R_o$:

$$\left.\begin{aligned} P(t) &= \tfrac{8}{3R_o}\int_{0^-}^{t} \psi(t-\tau)\tfrac{\partial a^3(\tau)}{\partial \tau}\,d\tau \\ \delta_1(t) &= a^2(t)/R_o \end{aligned}\right\} \quad \text{if } da(t)/dt \geq 0. \tag{5}$$

If the applied load is known, $a(t)$ is determined from Eq. (5) using Laplace transforms [18].

Case II is the interval between $t_{\max}$ and t', where a begins to decrease but is still larger than its initial value, a_o.

$$\left.\begin{aligned} P_{\mathrm{II}}(t) &= \tfrac{8}{3R_o}\int_{0^-}^{t_1(t)} \psi(t-\tau)\tfrac{\partial a_1^3(\tau)}{\partial \tau}\,d\tau \\ \delta_{\mathrm{II}}(t) &= \delta_1(t) - \int_{t_{\mathrm{peak}}}^{t} \phi(t-\tau)\tfrac{\partial}{\partial \tau}\int_{t_1(\tau)}^{\tau} \psi(\tau-\eta)\tfrac{\partial \delta_1(\eta)}{\partial \eta}\,d\eta\,d\tau \end{aligned}\right\} \quad \text{if } a(t_{\mathrm{peak}}) \geq a(t) \geq a_o \tag{6}$$

where $\partial\delta_1/\partial t$ is evaluated assuming Eq. (5) is valid beyond $t_{\max}$. These equations have two surprising features. First, the value of $a(t)$ at any t in the interval $t_{\max} < t < t'$ is determined entirely by the history of the contact *prior* to $t_1(t)$, the time at which a initially reached the same radius as at t. Second, the value of $\delta_{\mathrm{II}}(t)$ depends only on the history between $t_1(t)$ and t and is independent on the behavior *prior* to $t_1(t)$.

Finally, case III describes the behavior after a has decreased below a_o; *i.e.*, for $t \geq t'$,

$$\left.\begin{aligned} P_{\mathrm{III}}(t) &= \tfrac{8}{3R_o}\phi(t)a_1^3(t) \\ \delta_{\mathrm{III}}(t) &= \delta_{\mathrm{II}}(t') - \int_{t'}^{t} \phi(t-\tau)\tfrac{\partial}{\partial \tau}\int_{0}^{\tau} \psi(\tau-\eta)\tfrac{\partial \delta_1(\eta)}{\partial \eta}\,d\eta\,d\tau \end{aligned}\right\} \quad \text{if } a(t) \leq a_o \tag{7}$$

where a_1, δ_1 and δ_{II} are evaluated assuming Eqs. (5) and (6) are valid beyond $t_{\max}$. Equations (5)–(7) scale with R_o in the same way that the elastic Hertz results do; *i.e.*, $a \propto R_o^{1/3}$ and $\delta \propto R_o^{-1/3}$.

3. EXAMPLES

We now use the three simple mechanical models shown in Figure 3 to illustrate the effects of creep on the formation and rupture of

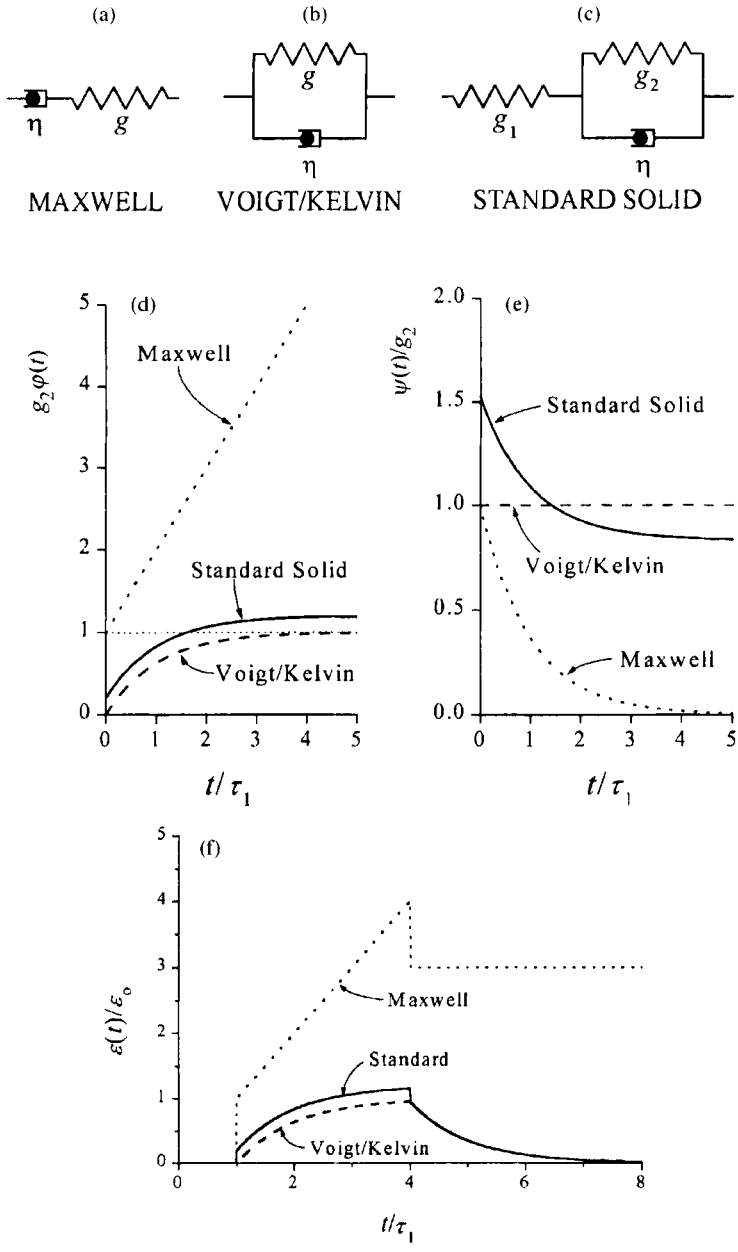

FIGURE 3 Simple mechanical models of linear viscoelastic response. (a) Maxwell model; (b) Voigt/Kelvin model; (c) Standard solid model; (d) Creep compliance functions; (e) Stress relaxation functions. (f) Strain following a step increase of stress at t/τ_1 and a step decrease at 4 t/τ_1.

contacts with nanometer-scale dimensions [26, 31]. The elastic elements are Hookeian springs each with shear modulus g. Each viscous element is a Newtonian dashpot with viscosity η. These mechanical models do not quantitatively describe actual polymers. However, they do capture the major features of the polymer response and, therefore, provide simple models that are useful for semi-quantitative analysis of data and for the design and interpretation of experiments. It is in this spirit that they are used here. Unless stated otherwise, specific examples shown below use the parameter values $g = g_2 = 2\,\text{MPa}$, $g_1 = 10\,\text{MPa}$, $\eta = 10\,\text{MPa}\cdot\text{s}$, with corresponding relaxation times (see below) of $\tau_M = \tau_{V'} = \tau_1 = 50\,\text{s}$ and $\tau_2 = 8.33\,\text{s}$.

The Maxwell model (Fig. 3a) consists of a spring and dashpot in series. Figures 1d and 3e show the creep compliance and stress relaxation functions

$$\left.\begin{aligned} \phi_M(t) &= (1 + t/\tau_M)/g \\ \psi_M(t) &= g\exp(-t/\tau_M) \end{aligned}\right\} \tag{8}$$

where $\tau_M \equiv \eta/g$ is the characteristic relaxation time following a step change in strain. The Maxwell model is fluid-like if the viscosity is small and solid-like if it is large. Figure 3f shows the strain response of the Maxwell model subjected to a sudden step increase in stress by σ_o at $t/\tau_1 = 1$ followed by a sudden decrease by $-\sigma_o$ at $t/\tau_1 = 4$. The instantaneous elastic response of the spring is followed by a linear response of the dashpot. When the stress is removed, the spring instantly relaxes but the dashpot remains extended; the Maxwell model can exhibit permanent deformation.

The Voigt/Kelvin model (Fig. 3b) has a spring and dashpot connected in parallel. The creep compliance and stress relaxation functions are

$$\left.\begin{aligned} \phi_V(t) &= (1 - \mathrm{e}^{-t/\tau_{V'}})/g \\ \psi_V(t) &= g(1 + \tau_V\delta(t)) \end{aligned}\right\} \tag{9}$$

where $\tau_{V'} \equiv \eta/g$ is the characteristic relaxation time following a step change in stress. Equations (9) are plotted in Figures 3d and 3e. The dashpot prevents any instantaneous elastic response. Unlike the Maxwell model, there is no permanent deformation (Fig. 3f).

The Maxwell model is a better approximation to the stress relaxation of polymers while the Voigt/Kelvin models better approximates creep response [31].

The standard solid model (Fig. 3c) is a three-parameter model that gives a better overall approximation to the response of polymers to changes in stress and strain. It consists of a Voigt/Kelvin model with parameters g_2 and η in series with an elastic spring g_1. The creep compliance and stress relaxation functions are

$$\left.\begin{aligned} \phi(t) &= \frac{1}{g_2}\left[\left(\frac{\tau_1}{\tau_1-\tau_2}\right) - \exp(-t/\tau_2)\right] \\ \psi(t) &= g_2\frac{(\tau_1-\tau_2)}{\tau_1}\left[1 + \left(\frac{\tau_1-\tau_2}{\tau_1}\right)\exp(-t/\tau_1)\right] \end{aligned}\right\} \tag{10}$$

where $\tau_1 \equiv \eta/g_2$ is the relaxation time following a step change in stress and $\tau_2 \equiv \eta/(g_1+g_2)$ is the relaxation time following a step change in strain; τ_1 is always greater than τ_2. Equations (10) are plotted in Figures 3d and 3e. There is an instantaneous elastic response due to g_1.

If the loading varies cyclically at frequency ω as in dynamical mechanical testing, the response is characterized by a complex modulus and phase lag. For example, the mechanical response to a strain and stress

$$\begin{aligned} \varepsilon(t) &= \varepsilon_o \exp(i\omega t) \\ \sigma(t) &= \sigma_o \exp i(\omega t + \delta) \end{aligned} \tag{11}$$

with amplitudes ε_o and σ_o is given by

$$G(\omega) = (\sigma_o/\varepsilon_o)\exp i\delta = G_1(\omega) + iG_2(\omega) \tag{12}$$

and

$$\tan\delta(\omega) = G_2(\omega)/G_1(\omega) \tag{13}$$

where G_1 is the storage modulus and G_2 is the loss modulus. $G_1(\omega)$ and $G_2(\omega)$ are related to $G(t)$ by

$$G_1(\omega) = \omega\int_0^\infty G(t)\sin\omega t dt \quad \text{and} \quad G_2(\omega) = \omega\int_0^\infty G(t)\cos\omega t dt. \tag{14}$$

Time scales of experimental creep data are converted into frequency scales using the relationship $\omega = 1/t$ [29].

The fraction of the maximum energy stored that is lost per cycle is $\Delta W/W = 2\pi \sin\delta$ which has its maximum value at ω_o, the frequency at which $\tan\delta$ is maximum. Figure 4 illustrates the typical frequency dependence of $G_1(\omega)$, $G_2(\omega)$ and $\tan\delta$ for the standard solid model with $g_1 = 1$ GPa, $g_2 = 1$ MPa and $\eta = 100$ MPa · s. For these parameters, $\tau_1 = 100$ s, $\tau_2 = 0.1$ s and $\omega_o = 0.316\,\mathrm{s}^{-1}$. This model has properties similar to a styrene-butadiene random co-polymer with glass transition temperature near room temperature [24, 32]. G_1 is smallest at low ω where the polymer has rubbery response and largest at high ω where the polymer has glassy response. At high frequency, the dashpot cannot respond and the system responds like an elastic spring with modulus $G_1(\omega \to \infty) \to g_1$. At low frequency, the dashpot can fully relax and the system again responds elastically but with modulus $G_1(\omega \to 0) \to g_1 g_2/(g_1 + g_2) \approx g_2$ if $g_2 \ll g_1$ as in the example. $\tan\delta$ peaks at $\omega_o = 1/\sqrt{\tau_1 \tau_2}$ where G_1 is beginning to increase rapidly.

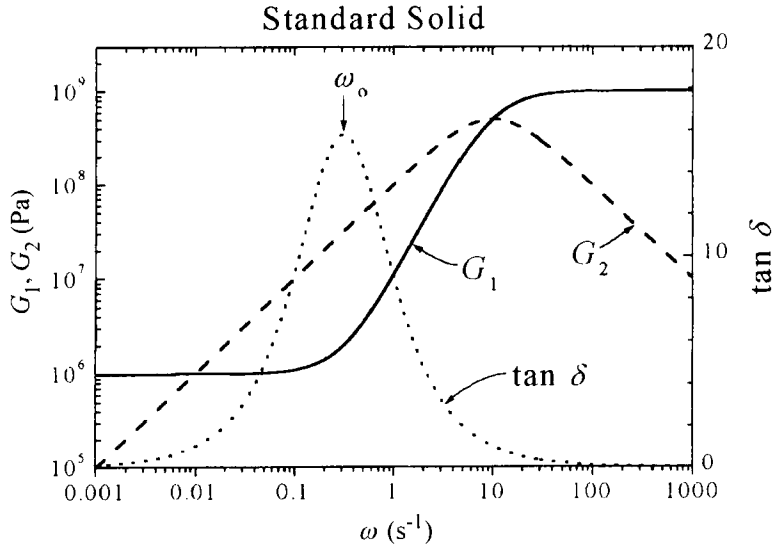

FIGURE 4 Frequency dependence of the storage modulus, G_1, loss modulus, G_2, and $\tan\delta$ for the standard solid model with $g_1 = 1$ GPa, $g_2 = 1$ MPa and $\eta = 100$ MPa · s ($\tau_1 = 100$ s, $\tau_2 = 0.1$ s and $\omega_o = 0.316\,\mathrm{s}^{-1}$).

Real polymers may have multiple peaks in tanδ. These peaks are frequently associated with excitation of particular molecular motions of the polymer, the glass transition temperature, or the melting temperature.

For the standard model, Figure 5 shows the interrelationships between the relaxation times, τ_1 and τ_2, the frequency, ω_o, and $\tan\delta_{max}$. The solid lines show the dependence of the maximum value of tanδ on τ_1 and τ_2 for $\tan\delta_{max} = 0.001$, 0.01, 0.1, 1, 10 and 100; *i.e.*, from nearly elastic to very dissipative materials. The diagonal dashed lines show the values of ω_o. The ranges of τ_1, τ_2 and ω_o were selected to span that generally accessible to SFM instruments. When reading the plot, it is important to keep in mind that $\tau_1 > \tau_2$, always. Highly

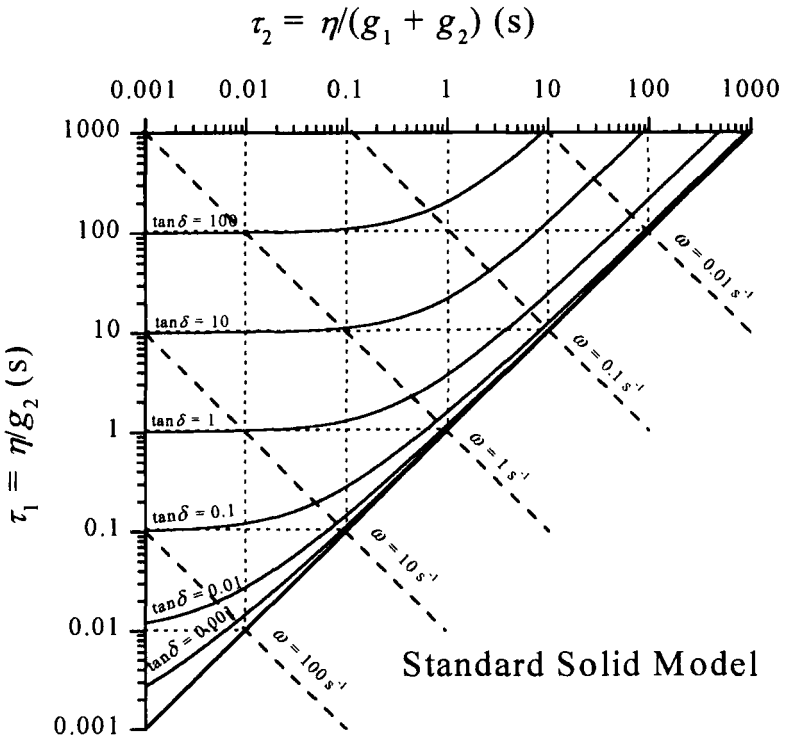

FIGURE 5 Dependence of $\tan\delta_{max}$ on τ_1 and τ_2 for frequencies accessible in SFM experiments. Solid lines are for $\tan\delta_{max}$ = 0.001, 0.01, 0.1, 1, 10 and 100. Dashed lines show the frequencies at which the maxima occur.

dissipative materials occur toward the upper left corner and more elastic materials toward the lower right diagonal edge. This type of plot is useful in selecting parameters to match the standard model to a particular set of data. For example, if τ_1 and ω_o can be estimated, then τ_1 and $\tan\delta$ can be determined directly from Figure 5. In the case of 1,2-polybutadiene [20], shear modulation measurements suggest $\tau_1 \approx 50\,\text{s}$ and $\tan\delta \approx 1$ so that $\tau_2 \approx 20\,\text{s}$ and $\omega_o \approx 0.03\,\text{s}^{-1}$.

In the following subsections, these mechanical models are used to demonstrate the ways creep can affect nanometer-scale contacts. The response is calculated using a time-dependent applied load (Fig. 6a) selected to be similar to the load variation in a typical SFM force-distance measurement. The total time of contact between the probe and substrate is t_{contact} and the time at which maximum load, $P_{\max}$, occurs is yt_{contact} where $0 < y < 1$. Typically in SFM, $y \approx 0.2 - 0.3$. The unloading time is $t_{\text{unload}} = (1 - y)t_{\text{contact}}$. The slopes of the loading and unloading curves can be varied independently which is not the usual case in SFM experiments. The probe shape is assumed to be a paraboloid of revolution as in Figure 1 with $R_o = 50\,\text{nm}$. For this probe shape and linear loading, the contact radius and deformation

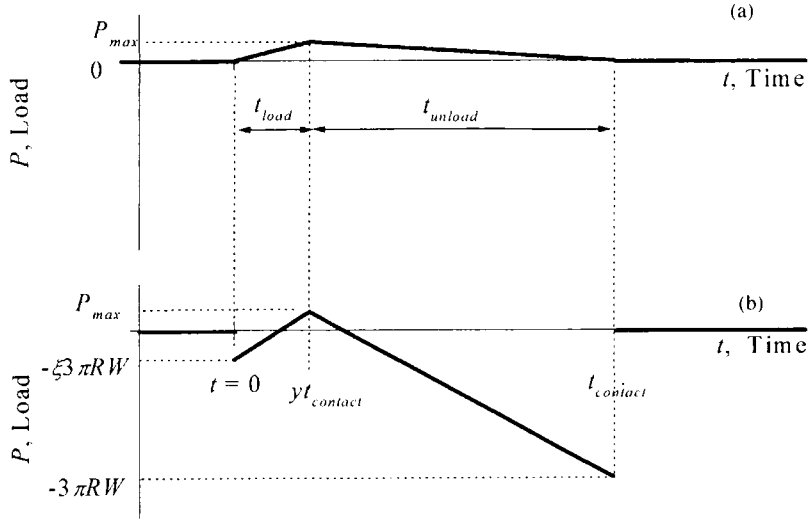

FIGURE 6 (a) Time-dependent linear loading ramp; (b) Time-dependent loading ramp with jump-to-contact and pull-off behavior.

scale as $a(t) \propto P_{max}^{1/3} R_o^{1/3}$ and $\delta(t) \propto P_{max}^{2/3} R_o^{-1/3}$. Thus, all the specific results presented below for $P_{max} = 2\,nN$ and $R_o = 50\,nm$ are easily extended to any other combination of P_{max} and R_o.

The choice of probe shape bears additional comment. A parabolic probe is frequently assumed for model calculations primarily for computational convenience. It is also the one choice made in all the commonly-quoted results from contact mechanics (Hertz, JKR, DMT, Barquins-Maugis, *etc.*) and, therefore, facilitates comparisons between viscoelastic and elastic materials. Additionally, a paraboloid is a good approximation to a sphere as long as the contact radius is much smaller than the sphere's radius ($a \ll R_o$). As an example, Figure 1a compares a parabola and sphere both with radius $R_o = 50\,nm$. However, as soon as a reaches $R_o/10$ or $R_o/20$, the paraboloid ceases to be a good approximation to a sphere. This condition is usually exceeded in SFM-scale experiments on compliant materials. Additionally, real SFM probes are generally neither parabolic nor spherical, except within about the first nanometer from the end [13]. Thus, for very compliant materials, which have $\delta \gg R_o$ even in the absence of an applied load [24, 33], the shape of the probe far from the end must be included if quantitative comparisons between experiment and theory are to be made. A conical probe shape may be a better choice [24, 33]. Incorrect choice of probe shape can have serious consequences. For example, in Hertzian contacts δ scales as $P^{2/3}$ for a parabolic probe, but as $P^{1/2}$ for a conical probe.

3.1. Maxwell and Voigt/Kelvin Models

We now use the Maxwell and Voigt/Kelvin models to illustrate some of the important characteristics of creep. These models are simple enough that the Ting equations [Eqs. (5)–(7)] can be solved analytically. In nearly all other cases, analytical solutions are not possible. Specific calculations below use $g = 2\,MPa$, $\eta = 100\,MPa \cdot s$ and $\tau_M = \tau_V = 50\,s$. These values are similar to those measured experimentally for 1,2-polybutadiene freshly cast from toluene solution [20, 21]. These models have behavior that brackets that expected for real materials.

Figure 7 shows the major features of the Ting solution for the Voigt/Kelvin model (Fig. 7a) and the Maxwell model (Fig. 7b). The contact radius, a, is plotted as a function of $t/t_{contact}$ for various

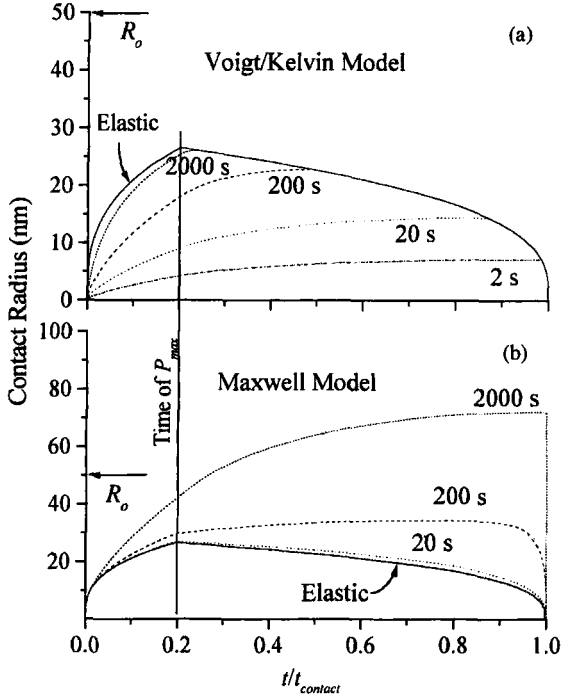

FIGURE 7 Solutions to the Ting model for contact of a rigid parabolic probe to a viscoelastic substrate described by (a) the Voigt/Kelvin model and (b) the Maxwell model.

$t_{contact}$. Each curve is labeled by its value of $t_{contact}$. The maximum load occurs at $y = 0.2$. Also shown for reference is the response of an elastic material with the same g (solid line). The most striking feature of both models shown in Figure 7 is that the time of maximum contact radius, t_{max}, does *not* coincide with the time of maximum load ($t = yt_{contact}$) as it does for elastic materials. Instead, maximum radius always occurs *after* the maximum load. This delay occurs because the substrate continues to respond by creep even during the unloading cycle.

Consider first the Voigt/Kelvin model (Fig. 7a). For finite contact times, the contact radius increases more slowly than in the elastic limit and its maximum value is always smaller. As $t_{contact}$ goes to values much shorter than τ, the response of the dashpot increasingly lags the applied load because $\tan\delta = \tau_V \omega_o \sim \tau_V / t_{contact}$. The contact becomes increasingly rigid, the maximum value attained by a becomes

smaller and smaller, and t_{max} shifts closer and closer to the end of the contact (*e.g.*, $t_{max} \rightarrow t_{contact}$) as shown Figure 8. Specifically,

$$t_{max} = -\tau_V \ln\left[\frac{y}{y - 1 + \exp(y t_{contact}/\tau_V)}\right], \tag{15}$$

i.e., t_{max} is a function of only (τ_V, y) and is independent of both P_o and R_o. The ordinate in Figure 8 is the fractional position of the peak in the unloading part of the cycle $(t_{max} - y t_{contact})$ normalized to the total unloading time $(t_{contact} - y t_{contact})$; it varies between zero and unity. For the Voigt/Kelvin model, y has little influence on the relative time in the unloading cycle at which maximum radius is reached. The total possible range of $0 \leq y \leq 1$ is shaded in dark gray in the figure. As $t_{contact}$ becomes much longer than τ_V, the dashpot is more responsive, and t_{max} decreases toward the time of maximum load; *i.e.*, the contact becomes more and more elastic. The most rapid variation of t_{max} occurs for $t_{contact}$ in the range $0.05\tau_V \lesssim t_{contact} \lesssim 5\tau_V$.

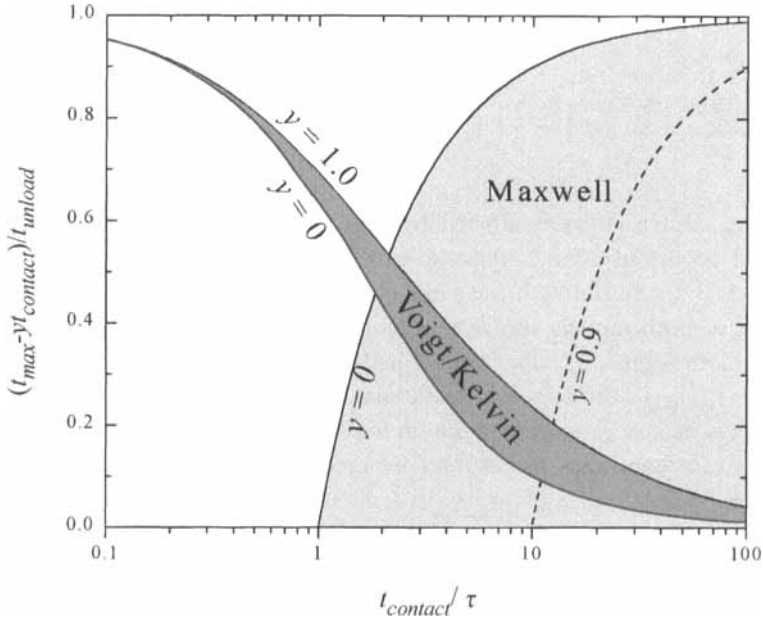

FIGURE 8 Relative time of the maximum contact radius in the unloading cycle as a function of $t_{contact}/\tau$ for the Maxwell and Voigt/Kelvin models. Adhesion is neglected.

In contrast to the Voigt/Kelvin model, the contact radius for the Maxwell model (Fig. 7b) is always larger than the elastic limit. In fact, $a \gtrsim R_o$ once $t_{\text{contact}} > \tau_M$ and this makes the more fluid-like Maxwell model more sensitive to the assumptions about the probe shape for a given (g, η). If $t_{\text{contact}} \leq \tau_M$, a has no delayed maximum. But as $t_{\text{contact}} \gg \tau_M$, the dashpot has more and more time to respond, the maximum reached by a becomes larger and larger, and t_{peak} moves closer to t_{contact} according to

$$\frac{t_{\max}}{t_{\text{contact}}} = 1 - \frac{\tau_M}{t_{\text{contact}}}; \tag{16}$$

i.e., the relative position of $t_{\max}$ is independent of y and depends only on τ_M. The relative location of $a_{\max}$ in the unloading cycle is compared with that of the Voigt /Kelvin model in Figure 8. The area shaded light gray indicates the full range of y values.

Experimentally it is desirable to have the maximum contact area occur in the middle of the unloading cycle since this region is isolated from the times of maximum loading and rupture where the maximum might be more difficult to distinguish. Examination of Figure 8 shows that this is generally possible if the maximum load occurs as soon as possible ($y \approx 0$) and if $t_{\text{contact}} \approx \tau$.

3.2. Standard Solid Model

The standard solid model is more representative of contacts to polymeric solids and exhibits behavior intermediate between the Maxwell and Voigt/Kelvin models. Johnson used the standard model to illustrate the time and load dependence of a from the viewpoint of the Ting model [17]. Typical response behavior is shown in Figure 9. The radius is confined between two limiting cases. For $t_{\text{contact}} \ll \tau_1$, the response approaches that of an elastic Hertzian contact of stiffness, g_1. For $t_{\text{contact}} \gg \tau_1$, it approaches that of an elastic Hertzian contact of stiffness $g_1 g_2/(g_1 + g_2)$. At intermediate t_{contact}, the behavior varies continuously between these limits. The contact radius, a, has the same delayed maximum behavior found for the simpler models. The relative time in the unloading cycle at which the maximum contact radius occurs is shown in

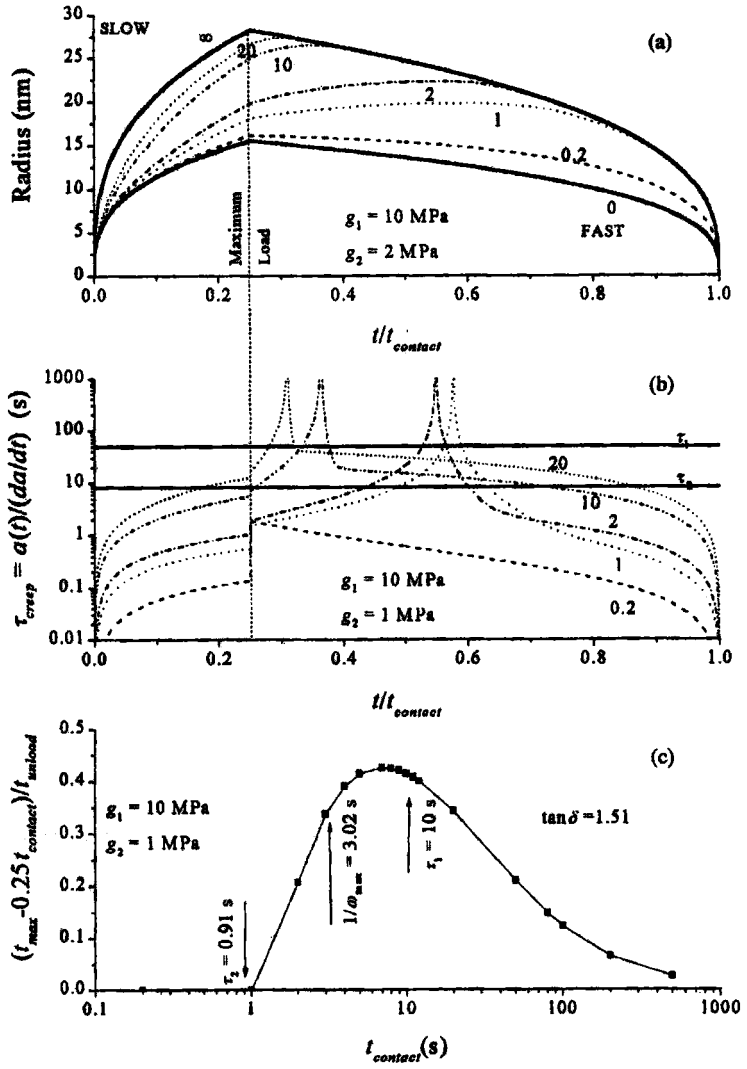

FIGURE 9 (a) Variation of the contact radius, a, for the standard solid model for $t_{\text{contact}}/\tau_1 = 0$, 0.2, 1.0, 2.0, 10, 20, ∞. The loading cycle is as in Figure 1a with $\nu = 0.25$ and $\eta = 10\,\text{MPa}\cdot\text{s}$; (b) $a(t)/(da/dt)$ for the same parameters as in (a); (c) Time in unloading cycle at which maximum contact radius occurs as a function of t_{contact}.

Figure 9c. The largest $t_{\max}$ occurs for $t_{\text{contact}} \approx \tau_1$. This time is close to $1/\omega_o$, the time at which energy dissipation has its maximum value.

Unfortunately, SFM measurements cannot directly determine the contact radius. Therefore, it is more important to examine the effects of creep on the deformation, δ, because this parameter can, in principle at least, be determined by SFM. Figure 10a shows P *vs.* δ obtained

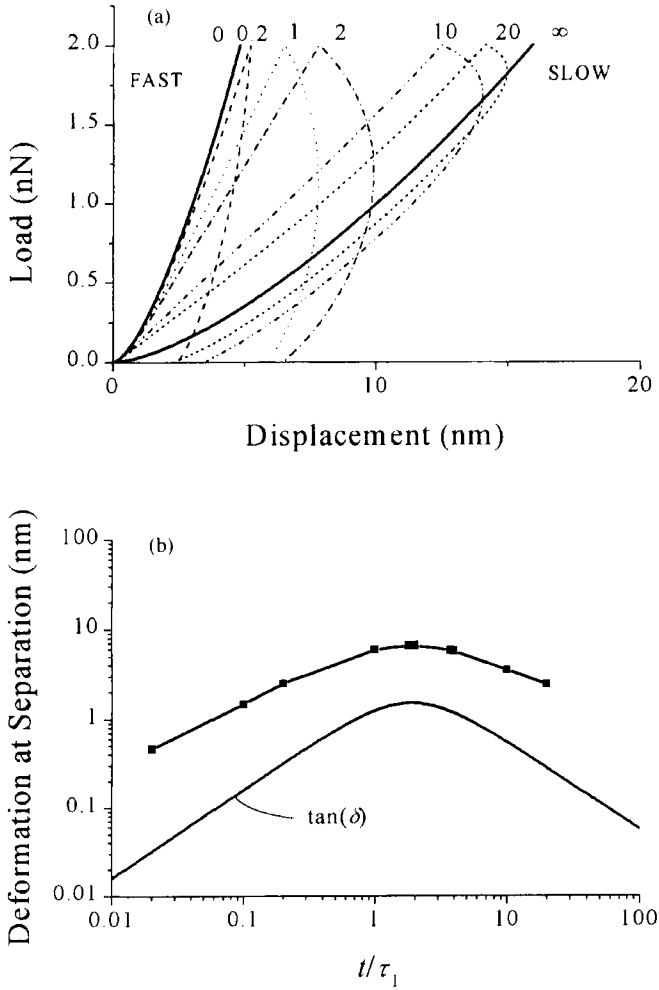

FIGURE 10 (a) Variation of the deformation, δ, with load for the standard solid model for various contact times, t_{contact}. Parameters are the same as in Figure 9a; (b) Variation of the deformation at separation with t_{contact} for the parameters in Figure 9a. Also plotted is tanδ where the frequency-to-time conversion has been made using $t = \pi/\omega$.

for the same parameters as in Figure 9a. The solid lines indicate the limiting elastic cases, which are reversible. The loading portion of the deformation curves shift continuously between these limits as $t_{contact}$ increases. As is the case for a, δ continues to increase after the load starts to decrease, *i.e.*, the probe tip continues to penetrate deeper into the substrate even though the load is decreasing. The maximum penetration is reached slightly after maximum a is reached. Separation of the probe and substrate at the end of loading (*i.e.*, $t = t_{contact}$ and $a = 0$) occurs well before δ can return to zero. The deformation at separation is plotted in Figure 10b and is largest when $t_{max} \approx 2\tau_1$. Also plotted in the figure is the loss tangent where the frequency has been converted to time assuming $t = \pi/\omega$ rather than the standard $t = 1/\omega$. Clearly, the maximum deformation at separation is correlated with the maximum energy dissipation and its shape, as a function of $t_{contact}$, is very similar to that of $\tan\delta$. The magnitude of the maximum deformation at separation is large, nearly 10 nm in this case. This large effect should be easily observable with SFM or other ultra low-load indention instruments.

3.3. Implications for Experiments on Viscoelastic Materials

These simple models provide a phenomenological framework for design and interpretation of experiments involving nanometer-scale contacts to viscoelastic materials. For example, the following general observations can be made:

1. The maxima attained by the contact radius, a, and deformation, δ, always increase as the contact time $t_{contact}$ increases.
2. The ranges on both a and can δ are bounded unless the polymer behaves more like a Maxwell fluid. The upper bound is set by the elastic response determined by the limiting value of the modulus at low frequencies. The lower bound is set by the elastic response as determined by the high frequency limit of the modulus.
3. Both a and δ attain their maximum values during the unloading for a large range of contact times. The maximum delay occurs when the contact time is approximately equal to the inverse of ω_o, the frequency at which $\tan\delta$ is maximum.

4. CREEP IN VISCOELASTIC CONTACTS WITH ADHESION

The discussion of creep given above completely ignores adhesion. Unfortunately, the contact mechanics problem for a viscoelastic material that includes both adhesion and creep has not yet been solved. Certainly, adhesion will increase the contact area, just as it does for elastic materials.

The boundary conditions on $z=0$, as given by Eq. (4), must be modified to include contributions to the radial pressure distribution, $p(r)$, from adhesion forces [16]. One possibility is to use

$$\sigma_{zz} = -p(r) = -\frac{\partial w(D)}{\partial D(r)} \quad \text{and} \quad \sigma_{rz} = 0. \tag{17}$$

everywhere at the interface, where $w(D)$ is the free energy of interaction between planar surfaces separated by D and might be approximated by Lennard-Jones or Dugdale potentials. This is the approach used by Hughes and White [34] and Barthel [16] to obtain a general solution to the equivalent elastic problem. Equation (17) is the Derjaguin approximation and is satisfied for SFM-scale contacts [12]. The adhesion energy, W, is related to w by [16]

$$W = -\int_0^{-\infty} \sigma(D)dD = \int_0^{-\infty} \frac{\partial w(D)}{\partial D} dD. \tag{18}$$

An alternative is to maintain the mixed boundary conditions of Eq. (4), but with $p(r)$ specified only for $r > a$:

$$\sigma_{zz} = 0 \rightarrow \sigma_{zz} = -p(r) \quad \text{for } r > a(t). \tag{19}$$

This approach has the advantage that only the attractive portion of w must be known. On the other hand, it assumes the spacing between the probe and substrate is constant everywhere inside the contact, usually estimated to be an interatomic spacing.

In the absence of an adequate theory, Tirrell and co-workers [35] have suggested an *ad hoc* approach to incorporate the effects of adhesion into the Ting model. In analogy with the Johnson, Kendall

and Roberts (JKR) [36] theory of adhesive elastic contacts, they simply replace the load in Eq. (5) with an effective load based on the JKR result, *i.e.*,

$$P(t) \rightarrow P_{\text{eff}}(t) \equiv P(t) + 3\pi W R_o + \sqrt{6\pi W R_o P(t) + (3\pi W R_o)^2}. \quad (20)$$

This substitution is expected to be valid only as long as the contact radius is increasing, since Eq. (5) applies only in this case. Equation (20) was found to give a good description of the increase in area of contacts between 0.7–1.2 mm diameter spheres of diblock copolymers of poly(ethylene)-poly(ethylene-propylene) [35]. In particular, the values of W extracted with this analysis were in excellent agreement with values determined by contact angle measurements [37].

Unertl extended this approach to include cases for which a is decreasing [26]. He used the Derjaguin-Muller-Toporov (DMT) limit $P_{\text{eff}}(t) = P(t) + 2\pi R_o W$ (see Fig. 6b), rather than the JKR limit, for analytical simplicity. In the case of the Maxwell model, the only effect is the expected increase in the contact radius. More importantly for the present discussion, there was no effect on the time lag at which the contact area reaches it maximum value. In the case of the Voigt/Kelvin model, the maximum value of the contact radius also increases. However, unlike the Maxwell model, $t_{\max}$ shifts toward shorter delay times, but by no more than ten percent. These results suggest that the major conclusions of the preceding section, particularly those shown in Figures 8 and 9c, will not be significantly altered by inclusion of adhesion. Specifically, inclusion of DMT adhesion appears to make only minor modifications to the Ting analysis for SFM-scale experiments.

A model proposed recently by Hui, Baney and Kramer incorporates adhesion and viscoelasticity [38]. The key feature of this model is the explicit realization that the cohesive zone at the crack tip must be finite in extent. This means that stresses are finite everywhere and, consequently, the rate of energy flow into the cohesive zone is dependent on the crack speed, da/dt. That is, unlike the case of elastic materials, the stress intensity factor $K(t)$ must be time dependent. Viscoelastic effects are described using the approach of Yang [39], which restricts the results to monotonically increasing contact area.

The contact area and deformation are expressed as

$$a^3(t) = \frac{3R}{4}\left\{\frac{3R\pi\phi_o^2 K_I^2(t)}{2} + \phi(t) * P(t) + \phi_o K_I(t) \sqrt{\left[\frac{3\pi R\phi_o K_I(t)}{2}\right]^2 + 3\pi R[\phi(t) * P(t)]}\right\} \tag{21}$$

and

$$\delta(t) = \frac{a^2(t)}{R} - \frac{K_I(t)\sqrt{\pi a(t)}}{\psi_o} \tag{22}$$

where ϕ_o is the short time compliance, ψ_o is the short time relaxation, $K_I(t)$ is the time-dependent Mode I stress intensity factor, and $\phi(t) * P(t) = \int_0^t \phi(t-\tau)(\partial P(\tau)/\partial\tau)d\tau$. $K_I(t)$ is eliminated from (21) and (22) using Schapery's solution for a closing crack [40], in which the cohesive forces are described by a Dugdale potential and the viscoelastic response by a simple creep compliance function

$$\phi(t) = \phi_o + \phi_1 t^m \tag{23}$$

where and ϕ_1 and m are constants. The long-time behavior of this model is fluid like. The rate of change of contact radius is given by

$$\frac{da(t)}{dt} = \frac{\pi K_I^2(t)}{8\sigma_o^2}\left[\frac{\phi_1}{\phi_o\lambda(Z)}\sqrt{\frac{\pi}{4}}\frac{\Gamma(m+1)}{\Gamma(m+3/2)}\right]^{\frac{1}{m}}\frac{1}{[1+\lambda(Z)]^2} \tag{24}$$

where

$$\lambda(Z) = \frac{2m+1}{4W(m+1)}\phi_o K_I^2(t)\left\{1 + \sqrt{1 - \frac{8Wm(m+1)}{\phi_o K_I^2(t)(2m+1)^2}}\right\} - 1. \tag{25}$$

For a load-controlled experiment, $P(t)$ is specified and Eqs. (24) and (21) or (22) are solved simultaneously to eliminate K_I and obtain the time variation of a and δ. For a displacement-controlled experiment, $\delta(t)$ is specified and Eqs. (24) and (21) or (22) are solved simultaneously to obtain the time variation of a and P.

Hui, Baney and Kramer show explicitly that Eq. (20), used by Tirrell and coworkers, is a misapplication of the correspondence principle and cannot be correct. In numerical simulations, they obtain reasonable fits to the data of Ref. [35] and also show that Eq. (20) overestimates $a(t)$.

The model used by Hui, Baney and Kramer requires a detailed knowledge of the local failure and bonding processes at the crack tip. This leads them to suggest that adhesive properties of contacts to viscoelastic materials are not best characterized by the work of adhesion, W, but rather by the stress intensity factor $K_I(t)$. The relationship between $a(t)$ and K_I, Eq. (24), is complex since $a(t)$ can depend on the entire history of K_I.

5. TIME SCALES IN SFM EXPERIMENTS

As discussed in the introduction, the creep and crack regimes can be distinguished by their relaxation times, τ_{crack} and τ_{creep}. In this section, the expected magnitudes of these relaxation times are estimated and the experimental regimes in which one is emphasized over the other are determined. Estimation of τ_{crack} for a viscoelastic material requires an estimate of the crack length, l, which can be obtained using the Dugdale interaction model [17, 41, 42], as follows.

The Dugdale model provides a more realistic description of the deformations near the contact periphery than does the JKR model. The pressures in the contact are compared for the two models in Figure 11 with the JKR model on the right and the Dugdale model on the left. The Dugdale interaction is also compared with a Lennard-Jones interaction in the insert on the left. The Dugdale interaction approximates the actual probe-substrate interaction force per unit area as a square well of depth, σ_o, and range, h_o. The work of adhesion is $W = \sigma_o h_o$.

In the JKR limit, the pressure in an adhesive contact between elastic bodies has two components, shown schematically on the right hand side of Figure 11. They arise from the external load and from the adhesion [14]. Superimposed on the figure (heavy lines) are the outlines of the substrate and parabolic tip as in Figure 1b. The Hertzian contribution from the external load (dashed line),

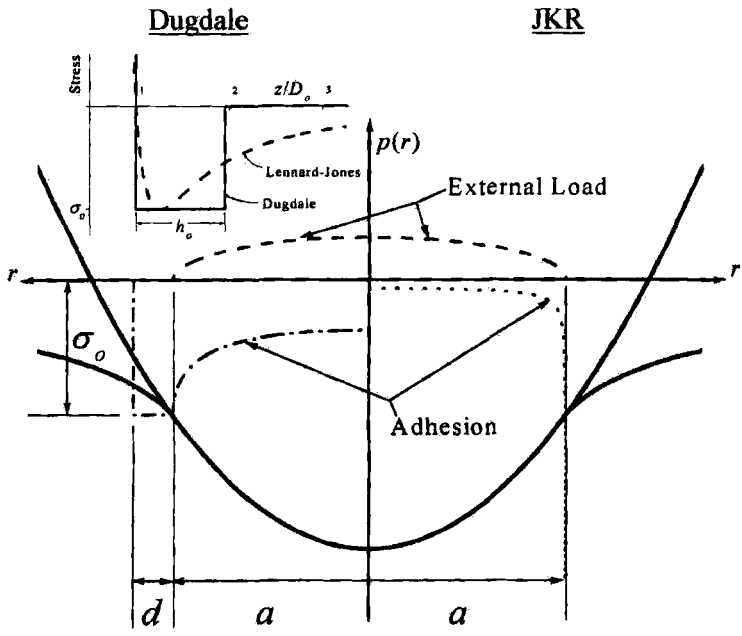

FIGURE 11 Comparison of the Dugdale and JKR models.

$P_{\text{external}}(r) \propto \sqrt{1-(r^2/a^2)}$, has the same form in both JKR and Dugdale models. It is largest in the center and falls to zero at the edges. In the JKR model, the adhesive contribution (dotted line) results in an additional contribution to the pressure, $p_{\text{JKR}}(r) \propto -1/\sqrt{1-(r^2/a^2)}$ where a now depends on the adhesion and, consequently, so does p_{external}. p_{JKR} is compressive and diverges strongly and unphysically at the periphery ($r=a$). This non-physical divergence is eliminated in the Dugdale model (dotdash line) where [10]

$$p_{\text{Dugdale}}(r) \propto \begin{cases} -\frac{2\sigma_o}{\pi}\tan^{-1}\sqrt{\frac{m^2-1}{1+(r/a)^2}} & \text{if } r < a \\ -\sigma_o & \text{if } a \le r \le a+d \end{cases}$$

where $m=(a+d)/a$. In both JKR and Dugdale models, it is clear that the dominant effects of adhesion occur at the contact periphery.

The lateral distance, d, over which the Dugdale force acts outside the contact defines the Dugdale zone. For a parabolic probe, d is

determined from [10]

$$h_o = \frac{4Wa}{h_o \pi E^*}\left[1 - m + \sqrt{m^2 - 1}\,\cos^{-1}\left(\frac{1}{m}\right)\right] + \frac{a^2}{\pi R_o}\left[\sqrt{m^2 - 1} + (m^2 - 2)\cos^{-1}\left(\frac{1}{m}\right)\right] \tag{26}$$

where $E^* \equiv \left[\left(1 + \nu_1^2\right)/E_1 + \left(1 + \nu_2^2\right)/E_2\right]^{-1}$ is the effective modulus and the subscripts refer to the probe and substrate. In the limit $d \ll a$,

$$d \approx \pi E^* h_o^2 / 4W \tag{27}$$

and is independent of R_o. (The equivalent expression given in Ref. [17] is incorrect.)

Creep and crack response are very different at the SFM-scale because l and a are very different. To show this, first consider a crack between elastic materials. Greenwood and Johnson [42], using the approach of Schapery [43], showed that the crack length, l, can be estimated as $l \approx E^* h_o^2 / 2W$. Comparing this with Eq. (27) shows that $l \approx 2d/\pi$. Thus, d is a reasonable estimate of the crack length and, in the following, we assume $l = d$. For viscoelastic materials, Greenwood and Johnson further showed that the same result holds but with E^* replaced $1/\phi(\tau_{\text{crack}})$. Thus, d/a is in the range $E^*_\infty h_o^2 / 2aW \leq d/a \leq E^*_o h_o^2 / 2aW$ where E^*_∞ is the limiting modulus for a slow moving crack ($\tau_{\text{crack}} \to \infty$) and $E^*_o \gg E^*_\infty$ is the limiting value for a fast moving crack ($\tau_{\text{crack}} \to 0$). Combining Eqs. (1) and (2), and using the JKR radius at pull-off ($a_{\text{pull-off}} = \sqrt[3]{9\pi W R_o^2 / 8E^*}$) as a convenient lower bound to a, yields

$$\tau_{\text{crack}} / \tau_{\text{creep}} < h_o^2 \left(\pi E_o^{*2} / 3W^2 R_o\right)^{2/3} \tag{28}$$

Equation (28) is plotted as a function of E^*_o in Figure 12 for the limiting combinations of W and R_o expected in SFM measurements. SFM probe tips have nominal radii in the range $10\,\text{nm} < R_o < 100\,\text{nm}$ and $10\,\text{mJ/m}^2 < W < 100\,\text{mJ/m}^2$ includes the range of W typically encountered in studies of polymer adhesion [44]. This analysis shows that $\tau_{\text{creep}} > 100\tau_{\text{crack}}$ for all materials with $E^*_o \leq 100\,\text{MPa}$, *i.e.*, the time scales are very different with τ_{creep} being significantly longer.

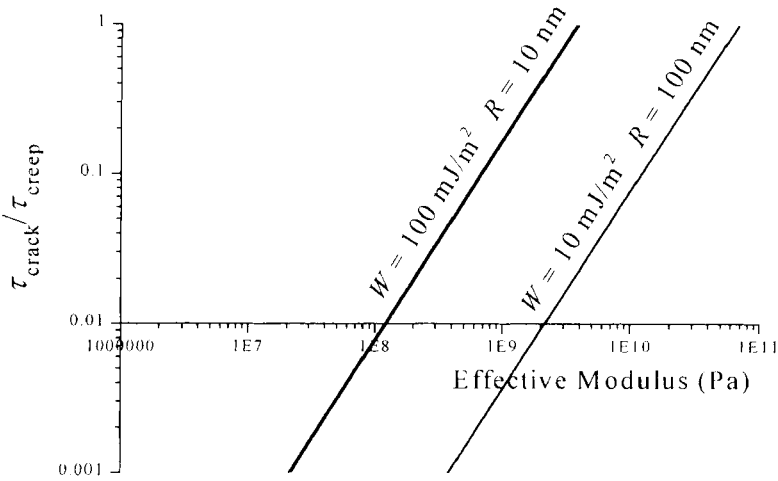

FIGURE 12 $\tau_{crack}/\tau_{creep}$ *vs.* E_o^*.

Since τ_{crack} and τ_{creep} are very different, it should be possible to study them separately. To do this, the SFM instrument must be able to satisfy two conditions. First, the characteristic relaxation time, τ, of the material under study must lie within the accessible range of experimental contact times, $t_{contact}$. Second, the experimental parameters must be adjusted so that either τ_{crack} or τ_{creep} is close to the characteristic relaxation time, τ of the sample under study. Using the approximations described above, the following expressions are obtained for *bounding* values of τ_{crack} and τ_{creep}

$$\tau_{creep} \geq a_{pull\text{-}off}/\langle V \rangle = \sqrt[3]{9\pi W R_o^2/8\langle V \rangle^3 E_o^*} \tag{29}$$

and

$$\tau_{crack} \leq d/V = \pi E_o^* h_o^2/4VW. \tag{30}$$

Note that τ_{crack} is independent of probe radius but $\tau_{creep} \propto R_o^{2/3}$. The bands of limiting values of Eqs. (29) and (30) that are shown in Figure 13 as a function of E_o^* were calculated for $\langle V \rangle = 100\,nm/s$ and $10\,mJ/m^2 < W < 100\,mJ/m^2$, and $10\,nm < R_o < 100\,nm$. For this range of parameters, the entire creep regime always lies above the band labeled "creep" and the crack regime lies below the band labeled "crack". Equivalent results for other choices of $\langle V \rangle$ are obtained by simply

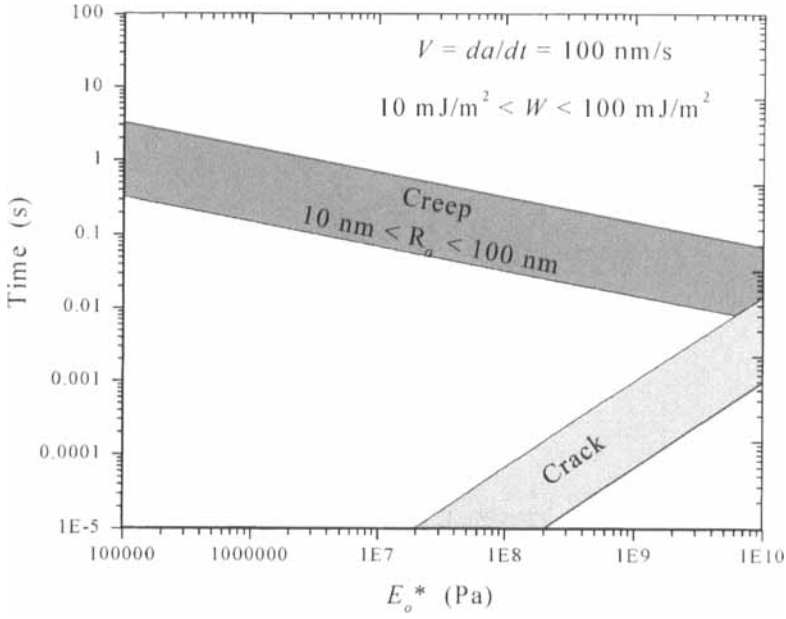

FIGURE 13 Creep and crack regimes accessible in SFM experiments for $\langle V \rangle = 100\,\text{nm/s}$.

shifting both bands vertically by $(100/\langle V \rangle)$ where $\langle V \rangle$ is measured in nm/s. For the example of Figure 13, creep effects are seen to dominate the SFM response for polymers with effective moduli below about 100 MPa and relaxation times in the range $0.1\,\text{s} \lesssim \tau \lesssim 10\,\text{s}$. Obviously, t_{contact} must lie in the same range as τ, which is the range used for the majority of force-distance curves reported in the literature. In order to bring the crack regime into this experimental range, V would have to be reduced by 3 to 4 orders of magnitude. SFM experiments have been done in this range by Basire and Fretigny [24] who measured the engulfment of an SFM probe into a styrene-butadiene random copolymer under zero load conditions. In this case, the increase in contact area is driven solely by surface forces and opposed by deformation of the substrate.

Tapping or intermittent contact mode [45] measurements involve very short contact times ($t_{\text{contact}} < 10^{-5}\,\text{s}$ or less) with very high $\langle V \rangle \gtrsim 10\,\mu\text{m/s}$. Again, creep effects will tend to dominate the measured response if the viscoelastic material also has $\tau \sim t_{\text{contact}}$.

In general, the creep regime is expected to dominate SFM measurements on compliant materials with $E_0^* \lesssim 100\,\text{MPa}$. For materials with higher moduli, the creep and crack regimes lie closer together and experiments are likely to be influenced by both. The requirement for low V and short t_{contact} makes it difficult for SFM to operate in the crack regime for most compliant materials. Unfortunately, this is the regime with the most complete theoretical model [11].

The discussion given above is presented in terms of average speeds, $\langle V \rangle$. V cannot be controlled in actual SFM instruments and it varies over a very wide range. Thus, in a real contact, the behavior will not be as simple as indicated by the arguments given above. This is illustrated in Figure 9b for the standard model where the instantaneous value of $\tau_{\text{creep}}(t) = a(t)/(da/dt)$ is plotted for the $a(t)$ results shown in Figure 9a. The relaxation times, τ_1 and τ_2, for the mechanical model are indicated by the solid lines. $\tau_{\text{creep}}(t)$ changes by over five orders of magnitude. It is very short during the initial stage of contact formation and in the final stages of pull-off so that the assumption $a \gg l$ may no longer be valid. At the point of maximum contact area, $\tau_{\text{creep}}(t)$ exceeds 1000 s. Its average value ranges between 5 s and 33 s as t_{contact} increases from $0.2\tau_1$ to $20\tau_1$. Even for the examples with the largest time lag to reach $a_{\max}$, $\tau_{\text{creep}}(t)$ is near τ_1 and τ_2 for a relatively small fraction of the total contact time.

6. SUMMARY

The theory developed by Ting [18, 19] has been applied to describe the contributions of creep to the response of nanometer-scale contacts during loading and unloading. This theory neglects the effects of adhesion but can be solved analytically for several simple models. None the less, it gives valuable insights into the behavior of small contacts. The major result is that creep can cause the contact area, a, and deformation, δ, to reach their maximum values well *after* the maximum load has been applied to the contact. Results obtained using simple mechanical models to describe the response of the viscoelastic materials provide useful guidance on how to optimize experiments to study creep. The maximum deformation at the instant the contact is broken is large and correlates well with the time dependence of the

loss function, tanδ. A typical SFM instrument should be able to study creep processes in materials whose characteristic relaxation times are in the range from roughly a millisecond up to a few hundred seconds.

Since the characteristic relaxation times of creep and crack regimes differ substantially for SFM experiments, the contact times of force-distance curves can be adjusted so that the response is by dominated one or the other.

Quantitative characterization of compliant viscoelastic materials requires that force *vs.* distance curves be carried out over as wide a range of contact times as possible. This observation should be particularly relevant for many biological materials where experimental contact times have been limited. Additionally, it suggests that studies of pull-off behavior that have traditionally relied on rather short contact times will need to be re-evaluated.

Most of the models described here are obviously too simple to be used for quantitative analysis of experimental data. However, most important differences are expected to be qualitative and the major conclusions reached using them will remain correct. The more rigorous analysis recently put forth by Hui, Baney and Kramer [38] correctly includes adhesion and creep, but only applies to cases where the contact size is increasing. It has not yet been applied to nanometer-size contacts. Once such an analysis becomes available, more complex systems such as layered films and living cells can be attacked quantitatively.

Acknowledgements

The author acknowledges financial support from the Department of Energy, the Office of Naval Research, the Paper Surface Science Program of the University of Maine, and the Maine Science and Technology Foundation. Discussions with K. L. Johnson and K. J. Wahl have also been invaluable.

References

[1] Burnham, N. A. and Colton, R. J., In: *Scanning Tunneling Microscopy and Spectroscopy*, Bonnell, D. A. Ed. (VCH Publishers, Inc., New York, 1993), p. 191.
[2] Hues, S. M., Draper, C. F. and Colton, R. J., *J. Vac. Sci. Technol.* **B12**, 2211 (1994).

[3] *Fundamentals of Friction: Macroscopic and Microscopic Processes*, Singer, I. L. and Pollock, H. M. Eds. (Kluwer Academic Publishers, Dordrecht, 1992).
[4] Colton, R. J., *Langmuir* **12**, 4574 (1996).
[5] Landman, U., Luedtke, W. D., Burnham, N. A. and Colton, R. J., *Science* **248**, 454 (1990).
[6] *Tribology Issues and Opportunities in MEMS*, Bhushan, B. Ed. (Kluwer Academic Publishers, Dordrecht, 1998).
[7] Mate, C. M., *Trib. Lett.* **4**, 119 (1998).
[8] You, H. X. and Yu, L., *Methods Cell Sci.* **21**, 1 (1999).
[9] Asif, S. A. A., Wahl, K. J. and Colton, R. J., *Rev. Sci. Instrum.* (1999).
[10] Maugis, D., *J. Colloid Interface Sci.* **150**, 243 (1992).
[11] Maugis, D. and Barquins, M., *J. Phys. D* **11**, 1989 (1978).
[12] Unertl, W. N., *J. Vac. Sci. Technol. A* **17**, 1779 (1999).
[13] Carpick, R. W., Agraït, N., Ogletree, D. F. and Salmeron, M., *J. Vac. Sci. Technol. B* **14**, 1289 (1996).
[14] Johnson, K. L., *Contact Mechanics* (Cambridge University Press, Cambridge, 1987).
[15] Savkoor, A. R., In: *Microscopic Aspects of Adhesion and Lubrication*, Georges, J. M. Ed. (Elsevier Sci. Publ. Co., Amsterdam, 1981), p. 279.
[16] Barthel, E., *J. Colloid Interface Sci.* **200**, 7 (1998).
[17] Johnson, K. L., In: *Microstructure and Microtribology of Polymer Surfaces*, Tsukruk, V. V. and Wahl, K. J. Eds. (American Chemical Society Books, Washington, D.C., 2000), p. 24.
[18] Ting, T. C. T., *J. Appl. Mech.* **33**, 845 (1966).
[19] Ting, T. C. T., *J. Appl. Mech.* **35**, 248 (1968).
[20] Wahl, K. J., Stepnowski, S. V. and Unertl, W. N., *Tribology Lett.* **5**, 103 (1998).
[21] Wahl, K. J. and Unertl, W. N., In: *Tribology Issues and Opportunities in MEMS*, Bhushan, B. Ed. (Kluwer Academic Publishers, 1999).
[22] Barquins, M. and Maugis, D., *J. Adhesion* **13**, 53 (1981).
[23] Barquins, M., *J. Adhesion* **14**, 63 (1982).
[24] Basire, C. and Fretigny, C., *C. R. Acad. Sci. Paris, Series IIb* **325**, 211 (1997).
[25] Kovacs, G. J. and Vincett, P. S., *Thin Solid Films* **111**, 65 (1984).
[26] Unertl, W. N., In: *Microstructure and Microtribology of Polymer Surfaces*, Tsukruk, V. V. and Wahl, K. J. Eds. (American Chemical Society Books, Washington, D.C., 2000), p. 66.
[27] Lee, E. H. and Radok, J. R. M., *J. Appl. Mech.* **27**, 438 (1960).
[28] Graham, G. A. C., *Int. J. Engng. Sci.* **3**, 27 (1965).
[29] Findley, W. N., Lai, J. S. and Onarian, K., *Creep and Relaxation of Nonlinear Viscoelastic Materials* (Dover Publications, New York, 1976).
[30] Savkoor, A. R., In: *Microscopic Aspects of Adhesion and Lubrication*, Georges, J. M. Ed. (Elsevier Science, Amsterdam, 1981), p. 279.
[31] Young, R. J. and Lovell, P. A., *Introduction to Polymers*, 2nd edn. (Chapman & Hall, London, 1991).
[32] Richard, J., *Polymer* **33**, 562 (1992).
[33] Domke, J. and Radmacher, M., *Langmuir* **14**, 3320 (1998).
[34] Hughes, B. D. and White, L. R., *Q. J. Mech. Appl. Math.* **32**, 445 (1979).
[35] Falsafi, A., Deprez, P., Bates, F. S. and Tirrell, M., *J. Rheol.* **41**, 1349 (1997).
[36] Johnson, K. L., Kendall, K. and Roberts, A. D., *Proc. R. Soc. London A* **324**, 301 (1971).
[37] Zhao, W., Rafailovich, M. H., Sokolov, J., Fetters, L. J., Plano, R., Sanyal, M. K., Sinha, S. K. and Sauer, B. B., *Phys. Rev. Lett.* **70**, 1453 (1993).
[38] Hui, C. Y., Baney, J. M. and Kramer, E. J., *Langmuir* **14**, 6570 (1998).
[39] Yang, W. H., *J. Appl. Mech.* **35**, 379 (1968).
[40] Schapery, R. A., *Int. J. Fracture* **39**, 163 (1989).
[41] Kim, K. S., McMeeking, R. M. and Johnson, K. L., *J. Mech. Phys. Solids* **46**, 243 (1998).

[42] Greenwood, J. A. and Johnson, K. L., *Phil. Mag.* **43**, 697 (1981).
[43] Schapery, R. A., *Int. J. Fracture* **11**, 369 (1975).
[44] Chaudhury, M. K., *Materials Sci. Engin. R* **16**, 97 (1996).
[45] Behrend, O. P., Oulevey, F., Gourdon, D., Dupas, E., Kulik, A. J., Gremaud, G. and Burnham, N. A., *Appl. Phys. A* **6**, S219 (1998).